Laminar wake suppression of airfoil by rotating rod at low Reynolds number

Yan Bao,* Huan Ping, Hongbo Zhu,† Dai Zhou,* Yuanfang Yang, and Zhaolong Han*
School of Naval Architecture, Ocean and Civil Engineering, Shanghai Jiao Tong University, Shanghai 200240, People's Republic of China

(Received 1 July 2021; accepted 22 February 2022; published 30 March 2022)

In this paper, the aerodynamic performance of an SD7003 airfoil with active control through momentum injection into the boundary layer is explored at a low Reynolds number of 5000. A two-dimensional incompressible flow is considered for the numerical solution of flow dynamics by employing the high-order spectral element method. The baseline airfoil cross section is modified with the presence of the rotating rod, which is placed at the suction side. The aerodynamic performance is extensively investigated in terms of mean and fluctuating components of lift and drag forces, lift-to-drag ratio, and control efficiency, as well for a range of rod location and rotational speeds for three attack angles of 4°, 8°, and 12°, respectively. Variation of flow pattern with a steady wake and unsteady shedding modes is then observed to be dependent on both the rotational speed and location. The numerical results indicated striking aerodynamic improvement at the condition of proper parameter combination, especially at incidence angles of 4° and 8°. Pressure drop and recovery at the upstream and downstream sides of the control rod, respectively, is found to be the primary mechanism for the lift enhancement and drag reduction. Proper orthogonal decomposition (POD) analysis on the instantaneous velocity field is carried out to illustrate the mode structure modification due to the control rod. The influence of spanwise effects is also tested for some representative cases by employing three-dimensional simulation, verifying the effectiveness of the current active method.

DOI: 10.1103/PhysRevFluids.7.034102

I. INTRODUCTION

Low-Reynolds-number (Re) aerodynamics of airfoils for the design of small-scale air vehicles, such as microair vehicles (MAVs), nanoair vehicles (NAVs), and picoair vehicles (PAVs) [1–5], has drawn increasing attention recently. According to the Defense Advanced Research Projects Agency (DARPA) specifications, MAVs are defined as small flying systems which are designed for working with a flow regime of $\mathrm{Re} = 10^4 \sim 10^5$; NAVs work at even smaller Re as low as 15 000, while PAVs operate at ultralow Re values, smaller than 3000. At such a flow condition of low Reynolds number, aerodynamic performance is quite sensitive to flow structure around airfoils, on which viscous force is dominated over the inertial force. Two different types of flight modes, the flapping mode and gliding mode, respectively, can be applicable for design of an effective airfoil at low Re conditions. While extensive investigations on flapping-type airfoils have been reported in the past [6–9], relatively little work has been dedicated to gliding-type airfoils so far. Inspired by dragonfly flight in gliding mode, highly corrugated wings were explored in the literature [10–13]. Another

*Also at State Key Laboratory of Ocean Engineering, Key Laboratory of Hydrodynamics of Ministry of Education and State Key Laboratory of Ocean Engineering and Collaborative Innovation Center for Advanced Ship and Deep-Sea Exploration, Shanghai 200240, People's Republic of China.
†hongbozhu@sjtu.edu.cn

 ©2022 American Physical Society

way to possibly achieve a higher performance of gliding at low Re is the flow control technique for typically applied airfoils at higher Re. For example, the Gurney flap, a simple passive control device fixed at the trailing edge, was found to be effective to modify the flow structure around an airfoil for improvement of aerodynamic characteristics at low Reynolds number. Mateescu *et al.* [14] numerically studied its effect on flow structure alteration of symmetric and cambered NACA airfoils at Re = 1000. More recently, Gopalakrishnan Meena *et al.* [15] reported that complex wake modifications behind NACA airfoils can be produced by a Gurney flap, which was evaluated in two-dimensional DNS simulations with companion three-dimensional simulations examining the spanwise instabilities on the wake mode transitions. A similar passively operating device of a rigid and flexible flap is also numerically tested in Fang *et al.* [16]. Their numerical results showed that at an optimal position of the short flap the lift-to-drag ratio can be improved up to 17.84% with significant suppression of lift and drag fluctuations.

Active control strategies, generally acting in a more efficient manner, have also received considerable attention. Among them, a moving surface is a favorable way to modify the wake characteristics of airfoils in terms of increasing the lift and delaying the flow separation. The first practical application of the moving surface for boundary-layer control to the airfoil was demonstrated by Favre [17]. Using an airfoil with the upper surface formed by a belt moving over two rollers, Favre [17] observed a significant delay of separation until the attack angle reached 55°. Modi *et al.* [18] later on introduced a similar concept in a wind tunnel study to examine its effectiveness. Their results showed that momentum injection through the moving surface can significantly delay flow separation within the boundary layer. In their experiment, cylinder rotation was utilized in the boundary layer and found to be beneficial for improving the stall characteristics of the Joukowsky model in a scenario of proper position. Al-Garni *et al.* [19] studied the increase of lift and decrease of drag for a NACA 0024 airfoil with simple trailing edge flap under the conditions of a low wind speed. Wind tunnel tests showed that if the rotating cylinder is close to the leading edge it would improve the lift coefficient and lift-to-drag ratio of the airfoil. With the high rotational speed of the cylinder, stall was also delayed. Du *et al.* [20] has carried out experimental research on the boundary-layer development and wake structure of a NACA 0015 airfoil with the presence of a rotating cylinder located at the leading edge. With the rotation of the cylinder, the separation of boundary-layer flow was delayed, the wake became narrower, and the lift coefficient was enhanced. The momentum thickness of the boundary layer was measured to decrease with the increase of cylinder rotational speed. Gerontakos and Lee [21] also studied the rotation effect of a cylinder close to the leading edge on the near wake of a NACA 0015 airfoil. Their results illustrated that, according to the rotational speed, the wake structure could be substantially modified, and several vortex-shedding modes appeared. It was also observed that the initial location of the Kármán vortex-shedding mode moved upstream with the increasing rotational speed of the cylinder. All these experimental investigations demonstrate that a rotating cylinder is an easy implementing solution of moving surface control. However, there is still an open question of how the control effectiveness varies with the cylinder position along the airfoil surface and how effective it is for flow conditions with low Re. More importantly, the associated flow physics involving the interaction between the rotating cylinder and the laminar boundary layer, which is responsible for the aerodynamic performance improvement of the airfoil, has not been well documented in the literature. However, studies on bluff body wake control by using rotating small cylinders [22–26] may shed some light on the underlying mechanisms. Schulmeister *et al.* [25] conducted a series of experimental studies at Re = 47 000 and reported that the drag force around the main cylinder is measured to reduce by 45% at the optimal rotation rate. In their complementary numerical simulation, the flow unsteadiness was fully suppressed in the wake at Re = 500 with the rotation rate being equal to 3. In addition, they found that the pressure recovery from the separation to reattachment points collapses with respect to a new scaling whereby they highlighted that it is the viscous effect that is the intrinsic control mechanism. This finding was further confirmed in Yu *et al.* [26], in which high-fidelity simulations for cylinder flow were conducted at Re = 3900 with two counter-rotating rods positioned close to the rear side

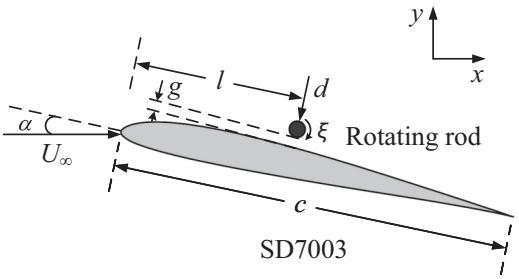

FIG. 1. Representative schematic view of an SD7003 airfoil at $\alpha = 8^\circ$ with a rotating rod of $d/c = 0.02$ and $g/c = 0.01$.

of the cylinder. Another question arising naturally is whether this pressure recovery mechanism also works for low Re airfoil control.

To address the aforementioned questions, we apply the rotating rod (or the small cylinder) from the wake control of a bluff body to an airfoil in the current investigation. We perform extensive simulations to explore the influence of a rotating rod position located in the boundary layer of the suction side of an airfoil on its aerodynamic characteristics. Pressure variation over the surface of the suction side is also explored to quantify the effects of control rod on flow dynamics in the boundary layer. A low-Reynolds-number airfoil with SD7003 cross section is chosen because of its wide availability in microair vehicles and unmanned air vehicles [27–30]. The Reynolds number considered is Re = 5000, which falls into the low-Reynolds-number range associated with small-scale air vehicles and ensures that the wake behind the baseline SD7003 airfoil is two-dimensional with laminar flow in the boundary layer. In these simulations, the rotational speed ratio is varied in a range from 0.0 to 4.0 for three different attack angles of 4°, 8°, and 12°, respectively. A broad range of parameter combinations results in the appearance of rich flow dynamics, but we mainly focus on investigating the effect of variations of rod position on aerodynamic control efficiency and flow behavior in the boundary layer. The paper is organized as follows: The computational approach and numerical setup are described in Sec. II, followed by the results of two-dimensional simulations presented in Sec. III. Three-dimensional simulations are supplementarily performed to examine the spanwise effects in Sec. IV. The findings are summarized at the end of the paper with a discussion on the prospects of potential applications.

II. PROBLEM FORMULATION

A. Flow configuration

We investigate the influence of a rotating rod located in the suction side boundary layer of an airfoil with SD7003 cross section on the aerodynamic performance at the chord-based Reynolds number of $\mathrm{Re}(\equiv cU_\infty/\mu) = 5000$ (here c is the chord length of the airfoil, U_∞ is the uniform inflow velocity, and μ is the fluid viscosity), which approaches the Re range of small-scale air vehicles [1–3,5]. The sketch of this problem is depicted in Fig. 1. The location of the rotating rod is denoted by nondimensional length l/c, which measures the distance from the leading edge of the SD7003 airfoil along the chord direction. The value of l/c is varied from 0.0 to 0.9 with an increment of 0.1, while the rotational speed ratio is defined as $\xi = U_s/U_\infty$, where U_s is the velocity on the rod surface and is normalized by the free-stream velocity, U_∞. In the simulation, the rotational speed ratio is varied from 0.0 to 4.0 with an increment of 1.0 at each location of the rotating rod. It is noted that further increase in ξ causes a significant rise of input power (the results are not shown here for sake of conciseness) and therefore the control efficiency would be deteriorated drastically. The majority of simulations were conducted at angles of attack of $\alpha = 4^\circ$ and 8°, but $\alpha = 12^\circ$, at which the laminar boundary layer separates approximately at the leading

edge of the airfoil, was also considered due to its massively separated nature of flow and high wake unsteadiness. The gap spacing between the rotating rod and the airfoil is fixed at $g/c = 0.01$, and the diameter of the rotating rod with respect to the chord length is set to a value of $d/c = 0.02$ for all the simulation cases. These values are much smaller when compared to those used in the cylinder wake flow control with rotating cylinders in Schulmeister *et al.* [25], so as to minimize the change of the original SD7003 geometry as much as possible. Keeping in mind that the control efficiency is sensitive to these parameters, a parametric analysis is of necessary interest in our future work.

B. Numerical method

The Navier-Stokes equations of the incompressible flow are employed for the description of fluid dynamics. The field variables of velocity and pressure are nondimensionalized by U_∞, ρU_∞^2, respectively, where ρ is the fluid density, while the length and time are by the chord length c and c/U_∞. The nondimensional form is expressed as

$$\frac{\partial \mathbf{u}}{\partial t} + (\mathbf{u} \cdot \nabla)\mathbf{u} = -\nabla p + \frac{1}{\mathrm{Re}}\nabla^2 \mathbf{u}, \tag{1}$$

$$\nabla \cdot \mathbf{u} = 0, \tag{2}$$

where $\mathbf{u} \equiv (u, v)$ [for three-dimensional (3D) simulations $\mathbf{u} \equiv (u, v, w)$] is the velocity vector, t is time, and p is pressure. The above equations are solved by a high-order spectral or *hp* element framework, NEKTAR++ [31,32]. For two-dimensional simulations, the computational domain is discretized into quadrilateral elements and the high-order modified Jacobian tensor-product polynomial shape functions are subsequently imposed on each macroelement. The spatial resolution is controlled by varying the order of polynomial expansion N_p, which is interpolated at the Gauss-Lobatto-Legendre quadrature points. For three-dimensional simulations, the spanwise evolution of the flow is resolved by introducing Fourier expansion as the discretization for the spanwise direction because the flow configuration possesses a spatial homogeneity in this direction.

A representative computational mesh for simulations at $\alpha = 4^\circ$ with $l/c = 0.8$ is depicted in Fig. 2. The airfoil is located in the C-shape computational domain with the domain length in streamwise direction being $16c$ with $6c$ ahead, the length in cross-flow direction being $12c$. The spanwise extent of the domain for three-dimensional DNS is chosen to be $L_z = 0.2c$. This span has been verified to be large enough to capture the spanwise evolution of wake flow in Uranga *et al.* [33] and Ducoin *et al.* [34]. The incoming flow is a uniform stream in simulations with a free-stream velocity of $(u, v) = (U_\infty, 0.0)$ imposed along the inflow boundary, and a free-slip condition ($\partial u/\partial y = \partial v/\partial y$=0.0) is specified on the far field boundary; a nonimpermeability condition is used on the wall of both the airfoil and rotating rod, while the velocity is left free using Neumann boundary conditions and the pressure is pinned to zero at the outflow. The spatial discretization in the x-y plane consists of a mesh with 11 679 quadrilateral elements (Fig. 2) with a polynomial order of $N_p = 4$. For 3D simulations, 48 Fourier complex modes are used to resolve the three-dimensionality in the spanwise direction.

C. Validation study

For the sake of the computational convergence, the efforts are made to conduct the mesh independence test by applying different orders ($N_P = 2$, 3, 4, and 5) of the polynomial expansion to each element. Considering the case with the parameter combination of $\alpha = 8^\circ$, $\xi = 3.0$, and $l/c = 0.75$, the statistical results are summarized in Table I with the mean coefficients of lift and drag, $\bar{C}_L$ and $\bar{C}_D$, and their root-mean-square values, C_L' and C_D', along with the Strouhal numbers, St. Here the lift and drag coefficients are defined as $C_L = \frac{F_y}{1/2\rho U_\infty^2 c}$ and $C_D = \frac{F_x}{1/2\rho U_\infty^2 c}$, F_x and F_y are the fluid force exerting on the airfoil surface in streamwise and cross-flow direction, respectively; the Strouhal number, i.e., the nondimensional form of the shedding frequency f_s measured from the time series of lift coefficient, is defined as $\mathrm{St} = \frac{f_s l^*}{U_\infty}$, in which l^* is the characteristic frontal length.

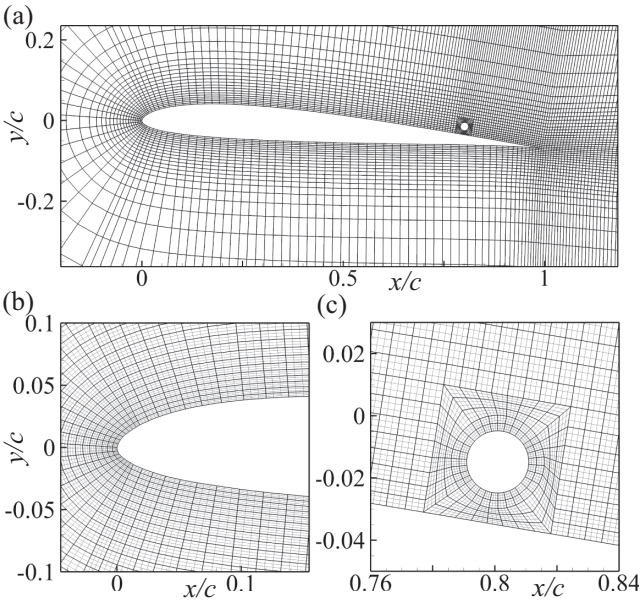

FIG. 2. Computational mesh with $\alpha = 4^\circ$ with $l/c = 0.8$ in the x-y plane: (a) detailed mesh around the SD7003 airfoil, (b) zoomed-in mesh around the leading edge with $N_p = 4$, and (c) zoomed-in mesh around the rotating rod with $N_p = 4$.

As Table I shows, with the increase in the polynomial order the relative errors decrease and are lower than 1% at $N_P = 3$ and 4. It is noticed that the global quantities of drag force, lift force, and Strouhal number are decreased a bit if N_P further increases from 4 to 5; however, the relative errors are only about 0.3%, showing good convergence properties of the simulations. The mean coefficients of drag and lift forces at Re = 10 000 obtained in both two- and three-dimensional (2D and 3D) simulations are further compared against the results in Uranga *et al.* [33], as tabulated in Table II. The difference in lift and drag coefficients relative to the 2D numerical simulations in Uranga *et al.* [33] is 3.52% and 1.79%, respectively. The difference is slightly decreased in the comparison made for 3D simulations. Therefore it can be concluded that the current investigation based on high-fidelity simulations has sufficient resolution to capture the aerodynamic force characteristics in low-Re regime.

In addition, the resolution of numerical results is further evaluated by comparing boundary-layer quantities of the displacement thicknesses, $\delta_1 = \int_0^\delta (1 - \frac{u_1}{U_1})d\mathrm{n}$, and momentum thicknesses, $\delta_2 = \int_0^\delta \frac{u_1}{U_1}(1 - \frac{u_1}{U_1})d\mathrm{n}$, of the isolated SD7003 airfoil in the time-averaged velocity field at Re = 5000 with the available data in literature [34]. Here δ is the boundary-layer thickness, u_1 is the normal

TABLE I. The mesh-independent test at Re = 5000. The relative errors (%) with respect to the results at $N_p = 5$ are shown in the parentheses.

N_p	$\bar{C}_L$	$\bar{C}_D$	C'_L	C'_D	St
2	0.6835 (9.78%)	0.1025 (13.58%)	0.6859 (10.05%)	0.1028 (13.69%)	0.2446 (1.92%)
3	0.7540 (0.48%)	0.1178 (0.67%)	0.7589 (0.47%)	0.1183 (0.67%)	0.2400 (0.00%)
4	0.7589 (0.17%)	0.1189 (0.25%)	0.7638 (0.17%)	0.1194 (0.25%)	0.2400 (0.00%)
5	0.7576	0.1186	0.7625	0.1191	0.2400

TABLE II. The comparison of mean drag and lift coefficients at Re = 10 000 ($\alpha = 4^\circ$). The differences (%) with the results in Uranga *et al.* [33] are shown in the parentheses.

Source	$\bar{C}_L$(2D)	$\bar{C}_D$(2D)	$\bar{C}_L$(3D)	$\bar{C}_D$(3D)
Uranga *et al.* [33]	0.3755	0.04978	0.3743	0.04967
Current	0.3892 (3.52%)	0.0489 (1.79%)	0.385 (2.78%)	0.0488 (1.78%)

profile velocity of the wall, and U_1 represents the free-stream velocity in the tangential direction of the wall. The comparison of the results is displayed in Fig. 3, showing that the displacement and momentum thicknesses in the case of $N_P = 4$ have minimal difference with those of $N_P = 5$ and are in agreement with the data from Ducoin *et al.* [34], especially the results of a fine mesh with $N_P = 6$. Considering both the efficiency and accuracy of simulations, $N_P = 4$ is applied to all the simulation cases, unless otherwise stated.

III. NUMERICAL RESULTS OF TWO-DIMENSIONAL FLOWS

A. Wake modes

Wake modes for an SD7003 airfoil without control are first visualized in terms of both instantaneous and time-averaged vorticity fields to serve as a reference baseline for the comparison purposes against the cases with control. As shown in Fig. 4, two different types of wakes are developed at Re = 5000, depending on the angles of attack considered: 2S and P mode. Here S and P stand for a single vortex and a vortex pair, respectively. Such a nomenclature of wake pattern is consistent with that observed for wake-vortex formation of an oscillating cylinder in Williamson and Roshko [35].

The 2S mode occurs at $\alpha = 4^\circ$, which is characterized by two alternatively counter-rotating single vortices in a shedding period. This mode then turns into the P mode when the attack angle increases to $\alpha = 8^\circ$. It can be seen that the streamwise separation between two vortex pairs in the P mode is larger than the 2S mode. In terms of the time-averaged vorticity fields shown in Fig. 4, the wake width, which is qualitatively measured as the distance between the two vorticity sheets elongated in the wake, has the same trend with the gap between two vortex pairs, as shown in the right column. In addition, the wake deflects to the lower side as it convects downstream in the 2S

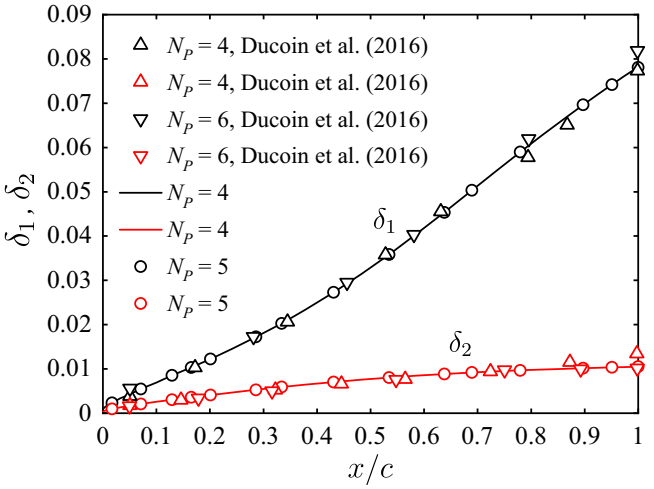

FIG. 3. Comparison of time-averaged displacement thickness δ_1 and momentum thickness δ_2 of SD7003 airfoil without the presence of the rotating rod at Re = 5000 with published data in Ducoin *et al.* [34].

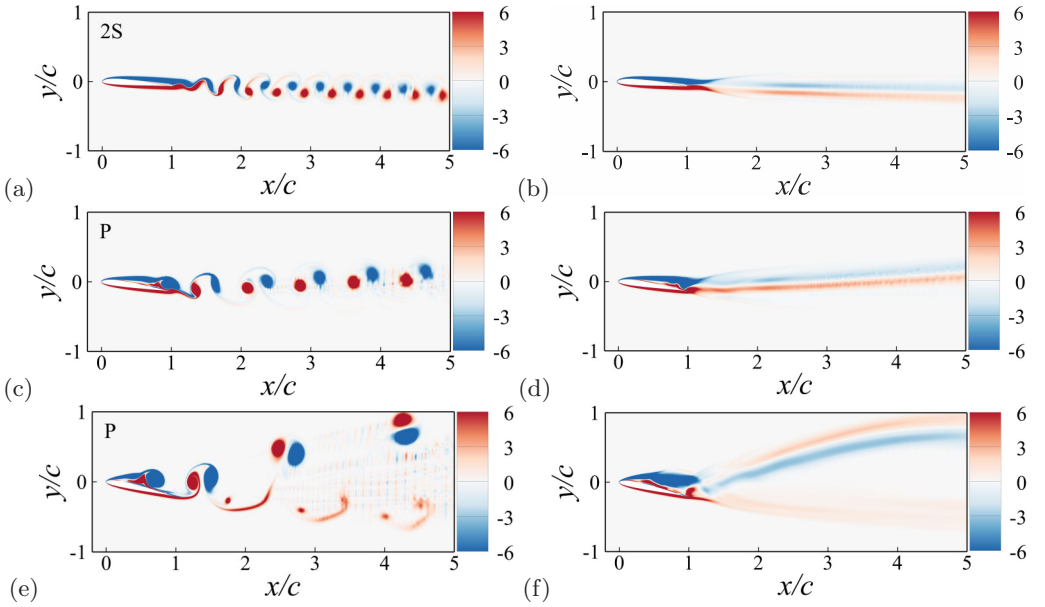

FIG. 4. Nondimensional instantaneous and time-averaged vorticity fields $\omega c/U_\infty$ of the SD7003 airfoil without the presence of the rotating rod at Re = 5000 with two characteristic wake-vortex modes, 2S and P: instantaneous vorticity fields with (a) $\alpha = 4^\circ$, (c) $\alpha = 8^\circ$, and (e) $\alpha = 12^\circ$; time-averaged vorticity fields with (b) $\alpha = 4^\circ$, (d) $\alpha = 8^\circ$, and (f) $\alpha = 12^\circ$.

mode, but for the P mode it deflects to the upper side instead, which is caused by the roll-up and subsequent shedding of the leading-edge vortex occurring in advance in this mode. Note that these two wake modes were also noticed for NACA0012 airfoils at Re = 1000 [15,36].

The rotating rod substantially modifies the wake mode, depending on the parameter combinations of rotational speed and rod location. Some typical wake modes are revealed for different angles of attack in Fig. 5, and the overall maps in the $(\xi, l/c)$ plane for $\alpha = 4^\circ$ and 8° are plotted in Fig. 6. Besides two unsteady wake patterns mentioned above, P+S mode is observed at $\alpha = 4^\circ$ with $(\xi, l/c) = (1.0, 0.2)$, where the airfoil periodically sheds a vortex pair and a single vortex, as shown in Fig. 5(d). Compared with the 2S mode at $(\xi, l/c) = (0.0, 0.5)$ depicted in Fig. 5(b), both the streamwise separation and the wake width in the P+S mode are much larger. Moreover, like the P mode, the wake of the P+S mode is biased to the upper side of the wake centerline. Apart from the wake modes of 2S, P, and P+S, a steady wake occupies the nearly upper-half region of the $(\xi, l/c)$ plane at $\alpha = 4^\circ$, which means that the rotating rod completely suppresses the wake unsteadiness and a steady state is achieved. For this scenario it is expected that enough momentum is injected into the shear layer that the shear layer reattaches to the suction surface of the airfoil and strengthens the ability to resist the adverse pressure gradient. With no subsequent occurrence of boundary-layer separation and vortex shedding, the steady regime contributes to the lowest drag coefficient compared with that in the other unsteady wake-vortex patterns, which will be shown later in Fig. 9(a).

The airfoil with the rotating rod of $\xi = 4.0$ depicted in Fig. 5(e) presents a 2S mode at $\alpha = 8^\circ$, whereas it changes into the P mode with the interference of a nonrotating rod. At the same attack angle, no matter how the location of the rotating rod, l/c, varies between 0.0 and 0.6, increasing rotational speed is always able to alter the mode gradually. As shown in Fig. 6(b), a typical 2S mode starts to appear at $\xi = 1.0$, and its occupied region expands wider and wider with further increase of rotational speed. From the comparison of these two maps in Fig. 6, it can also be observed that the 2S mode appears dominantly at the lower right side of the plane at $\alpha = 4^\circ$, whereas it moves to

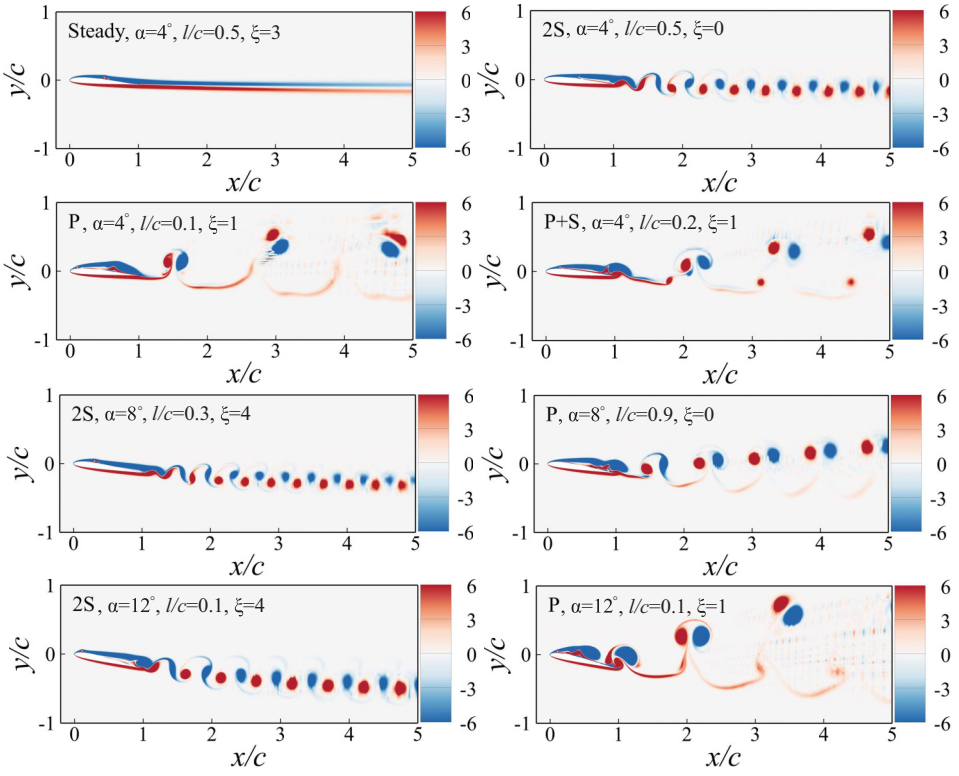

FIG. 5. Nondimensional instantaneous vorticity fields $\omega c/U_\infty$ for the selected cases at Re $= 5000$ showing four representative wake-vortex modes: steady, 2S, P, and P+S mode.

the upper left side at $\alpha = 8°$. This difference can be ascribed to the fact that flow separation occurs much earlier at the higher attack angle $\alpha = 8°$, and therefore the effective position of the rotating rod moves upward. A steady wake is not achieved even at the highest rotational speed considered for $\alpha = 8°$. In our supplementary case at $l/c = 0.6$ with $\xi = 8$, the wake is suppressed to a steady

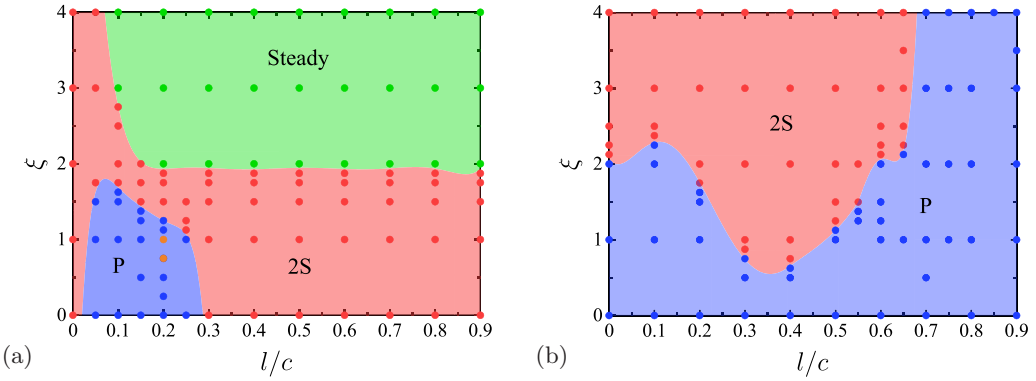

FIG. 6. Maps of the wake pattern for an SD7003 airfoil in the $(\xi, l/c)$ plane: (a) $\alpha = 4°$ and (b) $\alpha = 8°$. In the plot, green stands for steady mode, red for 2S mode, blue for P mode, and orange for P+S mode. The boundaries between the distinct wake patterns are obtained by polynomial curve fitting.

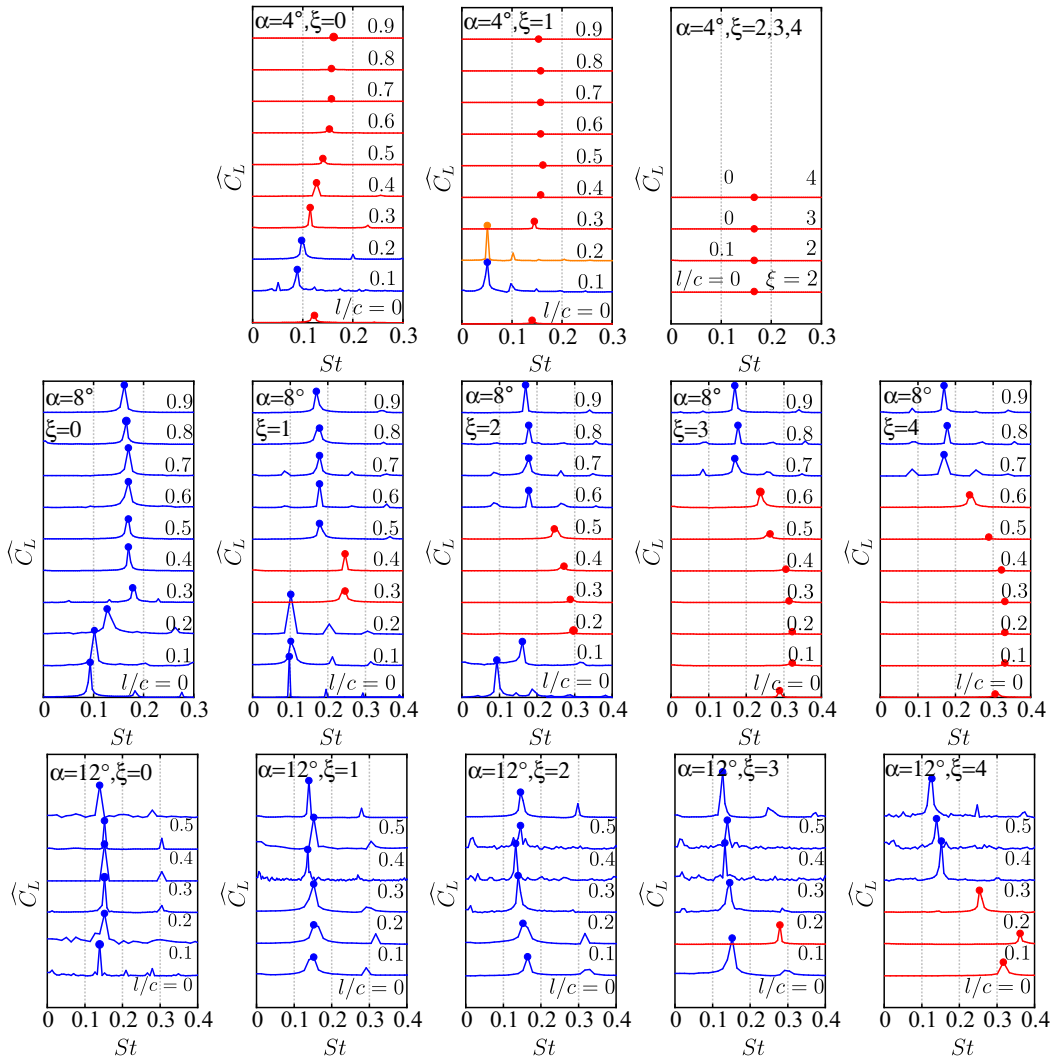

FIG. 7. The frequency spectra of lift coefficients for various α, ξ, and l/c. The • highlights the dominant frequency. Red, blue, and orange lines represent the 2S, P, and P+S mode, respectively. $\hat{C}_L$ stands for the power spectral density of the lift coefficient obtained through fast Fourier transformation over 100 vortex-shedding cycles.

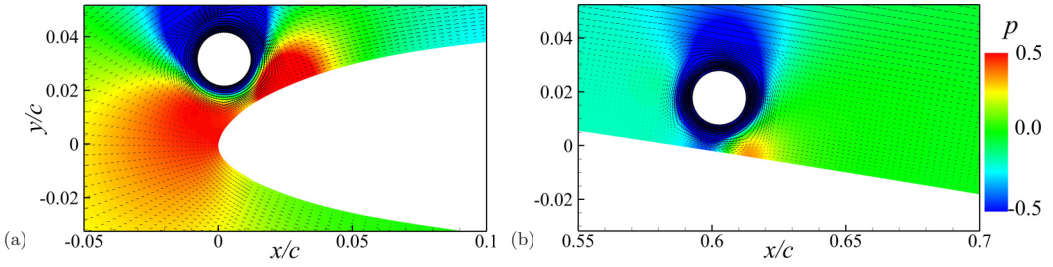

FIG. 8. Instantaneous velocity vectors and nondimensional pressure fields around the rotating rod of representative cases at Re = 5000, $\alpha = 4°$, and $\xi = 4$ with two different locations of the rotating rod: (a) $l/c = 0$ and (b) $l/c = 0.6$.

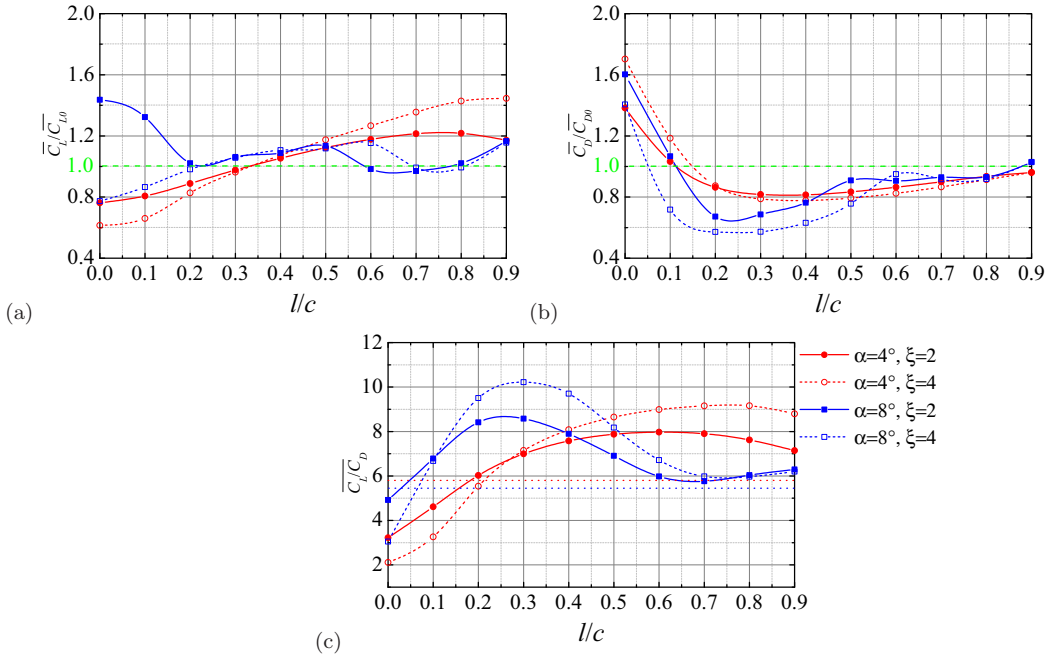

FIG. 9. Variation of the mean drag ($\overline{C_D}$) and lift coefficient ($\overline{C_L}$) and mean lift-to-drag ratio ($\overline{C_L/C_D}$) as a function of l/c for representative cases at $\alpha = 4^\circ$ and 8°: (a) $\overline{C_D}/\overline{C_{D0}}$, (b) $\overline{C_L}/\overline{C_{L0}}$, and (c) $\overline{C_L/C_D}$. The subscript $_0$ denotes the corresponding quantity for the baseline airfoil at the same α. The horizontal red and blue dashed line in (c) denote a value of $\overline{C_{L0}/C_{D0}}$ at $\alpha = 4^\circ$ and 8°, respectively.

state again (not shown here). However, such a high value of rotational speed would increase much of the input power, so it is out of the scope of the current discussion.

Note that the map for $\alpha = 12^\circ$ is not shown here because the majority of unsteady wakes at $\alpha = 12^\circ$ present the P mode pattern, which is similar to that found for the baseline airfoil at the same attack angle, indicating that the rotating rod hardly influences the wake dynamics at higher attack angle. The fact that the region corresponding to the 2S mode in the $(\xi, l/c)$ plane shrinks remarkably as compared with that at $\alpha = 8^\circ$ implies that the control effectiveness is deteriorated for massively separated flows from the leading edge of the airfoil. This observation is significantly different from the high efficiency of circular cylinder wake control as stated in Yu *et al.* [26] and Schulmeister *et al.* [25]. For the circular cylinder wake control, the rotating rod not only delays the flow separation but also attenuates the interaction of separated shear layers, resulting in efficient wake suppression even in the turbulent regime. In contrast, for the airfoil wake control, the rotating rod mainly imposes its existence in the boundary layer to resist the adverse pressure gradient; therefore its efficiency is weakened for massively separated flows at higher attack angles.

B. Frequency spectra

Frequency spectra of the sampling signal from the time history of lift force exerting on the SD7003 airfoil with the rotating rod are plotted in Fig. 7, with the red, blue, and orange lines representing 2S, P, and P+S mode, respectively. Note that since the frequency spectrum magnitude of lift coefficient is uniformly scaled, the dominant frequency marked in the plot seems to be undiscernible. In fact, as shown in the plot, at $\alpha = 4$ with variant rotational speeds the 2S wake is unsteady but in weak strength, and really peaks at a detectable dominant frequency. At $\alpha = 4^\circ$ and $\xi = 0.0$, a dominant vortex-shedding frequency is detected for the P mode, whereas the

vortex-shedding frequency associated with the 2S mode gradually shifts to higher frequency along with the reduction of peak value when the rod moves toward the trailing edge of the airfoil. For $\xi = 1.0$ there is a sudden change in the dominant vortex-shedding frequency occurring when l/c is increased from 0.2 to 0.3, which implies there is a transition of wake-vortex patterns to the 2S mode. However, the peak is hard to discern in the plot due to the significant suppression of wake oscillation for the 2S mode. At $\xi = 2.0$ the wake patterns for the locations of $l/c \in [0.2, 0.9]$ have eventually transformed into the steady regime without the formation of vortices; therefore no dominant frequency is detected in the spectra. It is interesting to emphasize that for the cases with the rotating rod quite close to the leading edge of the airfoil, for example at $l/c = 0.0$, increasing momentum injection ($\xi = 2.0$, 3.0, 4.0) cannot prevent the unsteady wake formation as shown in Fig. 7(c), which is because the rotating rod is located in the region of the favorable pressure gradient rather than the adverse pressure gradient, as can be seen in Fig. 8(a). Due to the clockwise rotation of the rod and the narrow spacing between the rod and wall ($g/c = 0.01$), the flow in the gap is completely upstream so that the rod in the favorable pressure gradient region shown in Fig. 8(a) will significantly affect the momentum growth of the boundary layer. More importantly, the angle between the tangential direction of the wall in the favorable pressure gradient region and the direction of the flow to be reattached to the wall is much larger than that in the adverse pressure gradient region shown in Fig. 8(b), which greatly increases the losses of momentum injected by the rotating rod. Therefore simply enhancing the speed ratio of the rod, like $\xi = 3.0$ or 4.0 in Fig. 7(c), has little effect on the value of St compared with that at $\xi = 2.0$. Figure 8(b) also clarifies how the rotating rod works to modify the pressure distribution through momentum injection. Specifically, a flow circulation is developed by the rotating rod, which carries along higher momentum around the rod and therefore a stagnation point is formed on the wall near the rear side of the rotating rod. This creates a positive pressure on the wall and thereby a favorable pressure gradient is established along the wall, causing the flow momentum to be streamed into the associated boundary layer further downstream. Such a significant rise of pressure on the wall is also verified in the pressure distribution at $l/c = 0.6$ with the same attack angle and rotating speed, as seen in Fig. 13(a).

For $\alpha = 8^\circ$ and 12°, with the increase in the characteristic frontal length, the dominant vortex-shedding frequencies for the developed wake-vortex patterns have a general increase compared with those at $\alpha = 4^\circ$. For instance, both of the maximum values of St for the 2S mode at $\alpha = 8^\circ$ and 12° exceed 0.3, which is much larger than that of St = 0.17 for the 2S mode at $\alpha = 4^\circ$. More interestingly, as the separation point of the boundary layer moves towards the leading edge of the airfoil, the free shear layer is getting further away from the wall of the airfoil so that the momentum cannot be directly injected into the free shear layer when the rotating rod is close to the trailing edge of the airfoil. Therefore, as we can observe from Fig. 7, the transition regions of wake-vortex patterns are getting narrower and closer to the leading edge of the airfoil as α increases. For $\xi = 4.0$ the transition regions l/c at $\alpha = 8^\circ$ and 12° are in the range of 0.0–0.6 and 0.0–0.2, respectively, which are distinctly narrower than that at $\alpha = 4^\circ$. Beyond that, it is clearly observed that for $\alpha = 8^\circ$ and $l/c \in [0.7, 0.9]$ with an interval of 0.1, it basically has no effect on the dominant vortex-shedding frequency as ξ increases from 3.0 to 4.0, which is exactly what happens when the momentum cannot be directly injected into the free shear layer.

C. Aerodynamic performance

Wake mode transition and spectral characteristics indicate that the rotating rod may have promising results for the improvement of aerodynamic performance of SD7003 airfoils in the low-Reynolds-number regime. In this section the effects of the control rod are further investigated by scrutinizing the statistics of global flow quantities, including the lift force, drag force, and the lift-to-drag ratio, in terms of both mean and fluctuating components. The numerical results are presented for two representative rotational speeds in order to reveal the essential features at attack angles of $\alpha = 4^\circ$ and 8°.

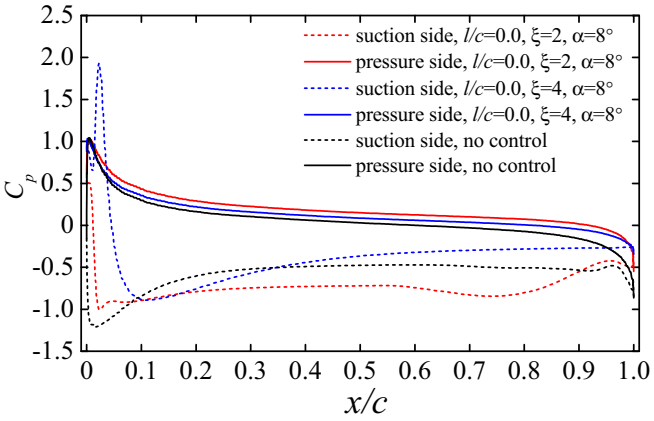

FIG. 10. The comparison of pressure coefficient distributions for two different rotation speeds ($\xi = 2$ and 4, respectively) at $l/c = 0.0$ and $\alpha = 8^\circ$. The results of the reference case without the control rod are also included.

In Fig. 9 we plot the variation of mean drag and lift forces (normalized with respect to that for the baseline airfoil without control) as a function of l/c. The lift-to-drag ratio is also plotted to indicate the aerodynamic efficiency of various configurations with the control rod. In Fig. 9(a) most of the curve is below the horizontal line which marks $\overline{C_D}/\overline{C_{D0}} = 1.0$, implying that drag reduction is achieved at $l/c \geqslant 0.2$. However, if the rod is located near the leading edge, for example, at $l/c = 0.0$, the drag force acting on the airfoil with the control rod is constantly larger than that for the uncontrolled case, no matter how large the rotational speed is within the range investigated here. The maximum drag reduction is achieved at $l/c = 0.3$ for an attack angle of $\alpha = 8^\circ$ when $\xi = 4.0$. For the case with $\alpha = 4^\circ$, the minimum value of the drag is noticed at $l/c = 0.4$, which is slightly larger than that for the case with $\alpha = 8^\circ$. The drag reduction effects are less pronounced with the increasing of l/c.

For a lower attack angle of $\alpha = 4^\circ$, the lift force increases monotonically with the increasing of l/c and exceeds a value of $\overline{C_L}/\overline{C_{L0}} = 1.0$ (see the horizontal line). In contrast, the curves at a higher attack angle of $\alpha = 8^\circ$ indicate a more complicated influence of the rod location on the lift force. If l/c is ranged between 0.0 and 0.2, the rotational speed has a distinct effect on $\overline{C_L}/\overline{C_{L0}}$. For instance, a significant lift enhancement is noticed at $\xi = 2$, while it is decreased with respect to the reference case at a higher rotating speed of $\xi = 4$. In order to explain the underlying reasons for this difference, we plot the pressure distribution along the surface at both the suction side and pressure side in Fig. 10. From this figure it can be seen that at this location the control rod has very little impact on the pressure side. On the contrary, the distribution on the suction side is greatly modified due to the rotating rod. At $\xi = 2$ the absolute value of pressure rises up significantly along the surface as compared with that for the uncontrolled case, which is responsible for the increase of lift at this rotational speed. When the rotational speed increases to a value of $\xi = 4$, the pressure changes impulsively in the region close to the leading edge, but its value settles down when $l/c > 0.1$, and therefore the lift is decreased accordingly at this speed. This observation indicates that the benefit of cambering for lift generation shrinks visibly due to the flow modulations at higher rotational speed. If the rod is located in the range of $0.2 \leqslant l/c \leqslant 0.5$, the curves for $\xi = 2.0$ and 4.0 nearly collapse toward each other, showing inconspicuous effects of rotational speed. If the control rod is close to the trailing edge, the lift falls into a trough region, which is slightly lower than that for the uncontrolled case.

The increase of $\overline{C_L}/\overline{C_D}$ indicates the improvement of aerodynamic performance of the airfoil, which is illustrated in Fig. 9(c). In the case of $\alpha = 4^\circ$, the ratio exceeds that of the baseline (red

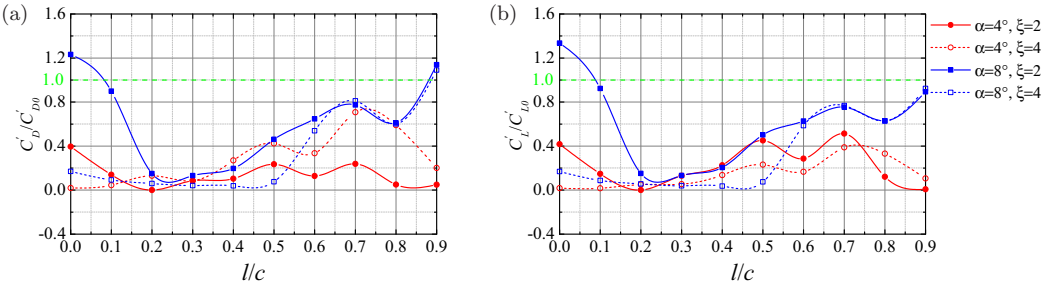

FIG. 11. Variation of the drag fluctuation (C_D') and lift fluctuation (C_L') as a function of l/c for representative cases at $\alpha = 4^\circ$ and 8°: (a) C_D'/C_{D0}' and (b) C_L'/C_{L0}'. The subscript 0 denotes the corresponding quantity for the baseline airfoil at the same α.

horizontal dashed line) approximately when $l/c > 0.2$ and reaches the peak value of 9.15 at $l/c = 0.8$ with $\xi = 4$, while the peak with a value of 10.22 occurs earlier, i.e., at $l/c = 0.3$, for the scenario when the attack angle increases to $\alpha = 8^\circ$. The lift-to-drag ratio is therefore increased by 86.50% for the case at $l/c = 0.3$ ($\xi = 4, \alpha = 8^\circ$), which is also much higher than the maximum value observed for flexible flap control (17.84%) [16], showing that a promising performance is achieved for active control via the rotating rod. The effective range of l/c is wider for $\alpha = 4^\circ$ with respect to that for $\alpha = 8^\circ$. Both lift enhancement and drag reduction contribute to the intrinsic improvement of the aerodynamic performance. However, the increase of $\overline{C_L}/\overline{C_D}$ for the lower attack angle of $\alpha = 4^\circ$ is mainly attributed to lift enhancement, while drag reduction dominates for the higher attack angle of $\alpha = 8^\circ$.

Fluctuation of the aerodynamic forces quantified through the root-mean-square value is also compared with the baseline case in Fig. 11. As shown in this figure, the fluctuation in both the drag and lift is suppressed or even totally disappears at $\alpha = 4^\circ$. This observation is in line with the wake suppression described in Sec. III A, which underlines the favorable properties with improved stability for low-Reynolds-number aerodynamics. At a higher attack angle of $\alpha = 8^\circ$, the control rod also displays promising aerodynamic performance along most of the chord, except for the location near the leading edge and trailing edge, where the control rod may amplify both the lift and drag fluctuations at a lower rotational speed. At $\xi = 4$ the drag and lift fluctuation is suppressed nearly 96.18% at $l/c = 0.4$ and 96.39% at $l/c = 0.4$, respectively, values which are also remarkably higher than the maximum values of 56.90% (drag fluctuation) and 40.90% lift fluctuation reported in Ref. [16]. It therefore may signify that active control is an efficient alternative with respect to passive control to improve the aerodynamic performance of a low-Reynolds-number airfoil.

To further investigate the influence of the control rod on the flow behavior within the boundary layer, the wall friction coefficient [$C_f = \tau_w/(0.5\rho U_\infty^2)$, where τ_w is the shear force] along the airfoil surface is plotted in Fig. 12. At $\alpha = 4^\circ$, the high-speed clockwise rotation of the control rod reverses the flow direction in the gap region, which is opposite to the main flow direction. Consequently, the flow separation occurs at the upstream position of the control rod around $x/c \approx 0.65$ and the jetlike flow with high velocity gradient is therefore generated in the gap region. As a result, the friction coefficient drops sharply to a value as low as –0.37 at the position $x/c = 0.7$. The entrapped flow by the control rod injects external momentum into the shear layer just in the downstream region of the control rod, leading to reattachment of the shear layer to the wall surface ($x/c \approx 0.72$), and as a result, C_f increases sharply. Further downstream, the kinetic energy loss of the fluid reduces the shear stress along the wall surface, which is revealed by the recovery of C_f to the level without a control rod. It is worth noting that the rotation of the control rod only affects the wall friction near the rod and basically has no effect upstream of the rotating rod. When α increases to 8°, the corresponding C_f distribution along the surface has a similar trend as that at $\alpha = 4^\circ$, except that the C_f peak moves to the position at $x/c = 0.3$. In summary, the rotating rod causes abrupt changes in

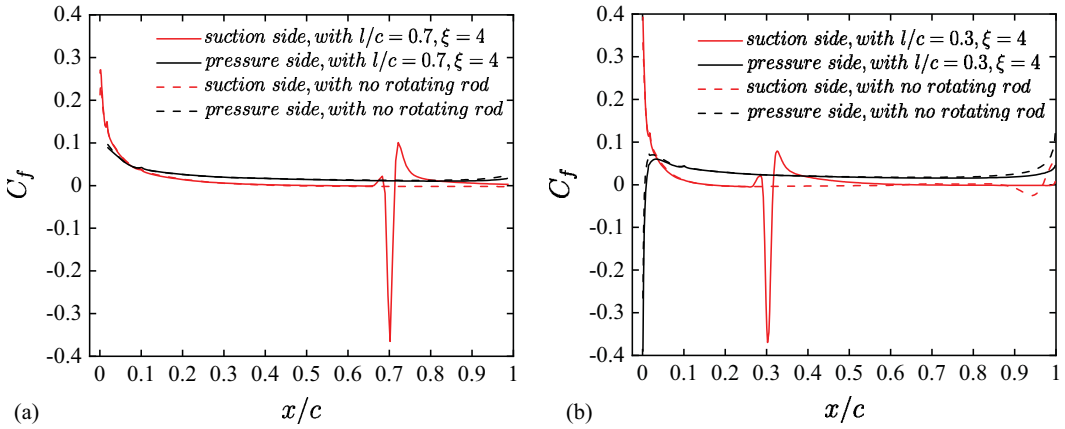

FIG. 12. The distributions of wall friction coefficient along the surface of SD7003 airfoil for control cases at (a) $\alpha = 4^\circ$ with $l/c = 0.7$ and $\xi = 4$, (b) $\alpha = 8^\circ$ with $l/c = 0.3$ and $\xi = 4$.

the wall friction locally but has little effect at other positions, and the difference in C_f corresponding to different wake modes is only shown at the airfoil trailing edge as displayed in Fig. 12(b).

Figure 13 illustrates how the pressure coefficient $[C_p = (p - p_\infty)/(0.5\rho U_\infty^2)]$ is modified along the surface on the suction side. The pressure magnitude significantly increases (more negative) in the upstream side of the control rod with respect to the case without a control rod. The amplified suction pressure upstream of the control rod is mainly ascribed to the accelerated flow velocity with the aid of a control rod, which is verified clearly in Fig. 14(b). The increase of the pressure suction therefore mainly contributes to the lift enhancement of the airfoil. On the other hand, pressure recovery is observed in the downstream side of the airfoil. Such a behavior is well documented as a drag reduction mechanism of a cylinder wake [25,26], which is applicable for the low-Reynolds-number aerodynamics of the airfoil. The pressure redistributed in a similar form at $\alpha = 8^\circ$; however, it is also noticed that the pressure recovery region is elongated much wider with respect to the case at $\alpha = 4^\circ$. As a result, the drag reduction effect becomes much more profound at $\alpha = 8^\circ$. The velocity field at $\alpha = 8^\circ$ is also seen in Fig. 14(d), showing acceleration of the flow at the upstream side of the control rod and a thinning boundary layer at the downstream side.

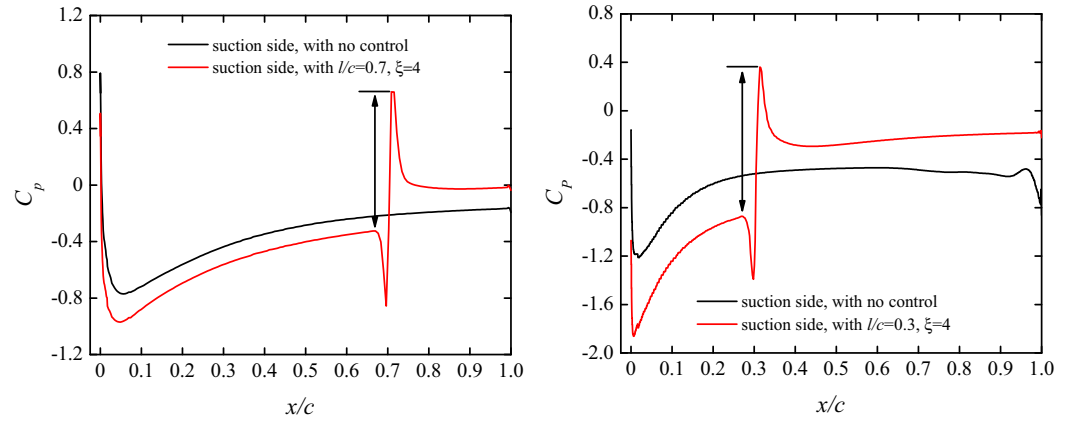

FIG. 13. The comparison of pressure coefficient distributions with and without control at (a) $\alpha = 4^\circ$ and (b) $\alpha = 8^\circ$.

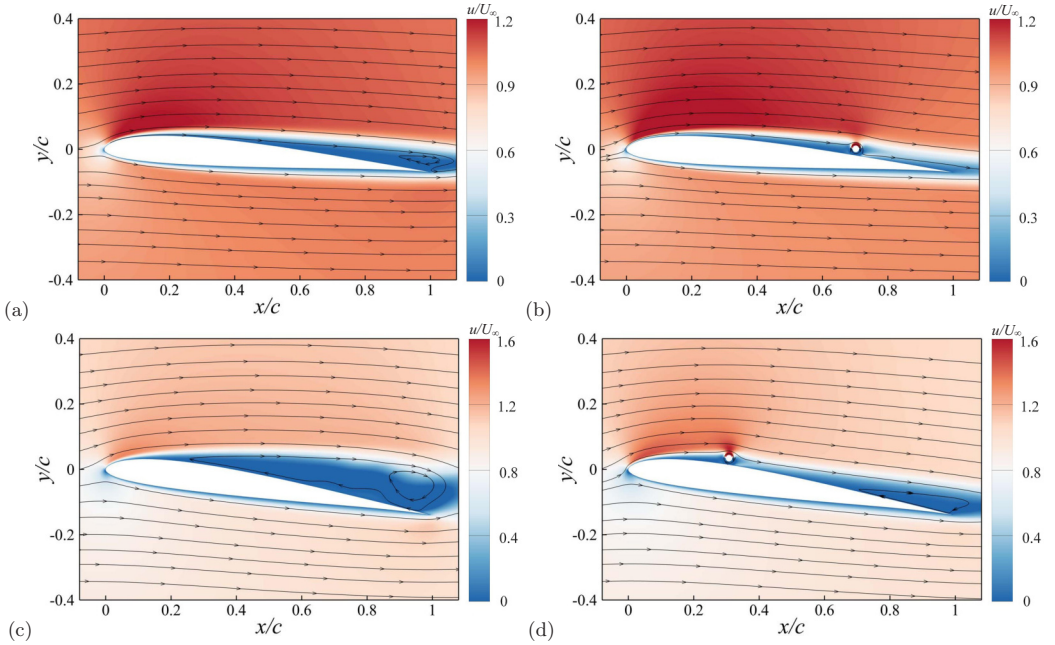

FIG. 14. The distribution of time-averaged streamwise velocity around an SD7003 airfoil at (a) baseline case at $\alpha = 4^\circ$, (b) control case at $\alpha = 4^\circ$ with $l/c = 0.7$ and $\xi = 4$, (c) baseline case at $\alpha = 8^\circ$, and (d) control case at $\alpha = 8^\circ$ with $l/c = 0.3$ and $\xi = 4$.

D. Control efficiency

The active control of rotating rod needs external power to maintain continuous momentum injection into the airfoil boundary layer; therefore it is necessary to study the associated power consumption of control with a rotating rod. It is noted that for active control of wake flow over a circular cylinder, the saved energy due to drag reduction can be estimated by comparison of the drag force from the counterpart of that without control. However, for the aerodynamics of an airfoil, changing power consumption due to lift enhancement should be taken into account. It is therefore rational to evaluate the control efficiency under the condition that the airfoils with or without the control rod experience equal lift force. Thereby, the total lift force (F_L^T) for the case with control can be first obtained with $F_L^T = F_L^{c,a} + F_L^{c,r}$ (where $F_L^{c,a}$ and $F_L^{c,r}$ represent the lift forces acting on the airfoil (a) and the control (r) rod, respectively). Subsequently, according to the condition $F_L^T = F_L^n = 0.5C_L^n\rho(U_\infty^n)^2c$, where F_L^n is the lift force acting on the reference airfoil, and then the free-stream velocity is updated as $U_\infty^n = \sqrt{F_L^T/0.5C_L^n\rho c} = \sqrt{F_L^n/0.5C_L^n\rho c}$. Therefore the value of corresponding drag force is obtained as $F_D^n = 0.5C_D^n\rho(U_\infty^n)^2c$. Finally, the saved power is estimated simply by $C_{\text{pow}}^{\text{sav}} = (F_D^nU_\infty^n - F_D^TU_\infty^c)/(0.5\rho U_\infty^3c)$ (here $U_\infty^c = U_\infty$, and the total drag on the control system is contributed from both the airfoil and the rotating rod, i.e., $F_D^T = F_D^{c,a} + F_D^{c,r}$). It should be noted here that the superscript n and c in the above variables stand for the case with no control and with control, respectively. The rotational power consumption coefficient is defined as $C_{\text{pow}}^{\text{rot}} = T\omega/(0.5\rho U_\infty^3c)$, where T is the torque exerting on the rod, and ω is the angle velocity of the rotating rod. In the following, the cases at $\alpha = 4^\circ$ with $\xi = 2$ and $\xi = 4$ are chosen to test the power-saving effectiveness through comparison of $C_{\text{pow}}^{\text{rot}}$ and $C_{\text{pow}}^{\text{sav}}$ for variation of the rod location in Fig. 15, which shows that the active control of a rotating rod is efficient at lower rotation rate ($\xi = 2$), as evidenced by the fact that the rotational power input is smaller than the saved power when x/c approximately ranges from 0.43 to 0.87 due to drag reduction in the condition of the same

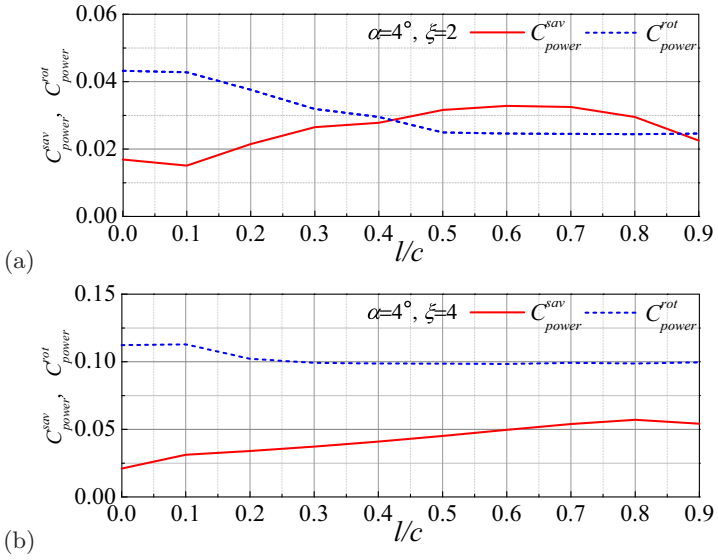

FIG. 15. Saved power and rotational consumption power for the cases of (a) $\alpha = 4^\circ$, $\xi = 2$ and (b) $\alpha = 4^\circ$, $\xi = 4$.

lift force with the reference case. For the higher rotation rate of $\xi = 4$, $C_{\text{pow}}^{\text{rot}} \geqslant C_{\text{pow}}^{\text{sav}}$ holds for all the rod locations, showing that power-saving effectiveness is deteriorated at higher rotation speeds. It should be noted that in a practical scenario we could not expect such a high efficiency due to energy loss caused by internal friction and so on.

E. POD analysis

With the objective to explore its underlying control mechanism, we resort to proper orthogonal decomposition (POD) for further analyses. In view of the aerodynamic characteristics of the SD7003 airfoil at a representative attack angle $\alpha = 8^\circ$ as shown in Fig. 9, optimal control is achieved at $l/c = 0.3$ and $\xi = 4$, in which the lift-to-drag ratio reaches the highest value. This case is therefore chosen as the typical case for POD analysis. A total of $N = 800$ snapshots of the fluctuating streamwise velocity field with a temporal spacing of 0.016 time units are processed using the algorithm described in Ping *et al.* [37]. The corresponding results of flow past a plain SD7003 airfoil without the presence of the control rod are also included to serve as a baseline case for comparison. For this case a total of $N = 750$ snapshots with a temporal spacing of 0.034 time units are adopted. Note that N is large enough in two cases to ensure the POD results to be well converged.

Figure 16 displays relative and cumulative energy distributions of POD modes. It is noted that the pairing phenomenon between two consecutive modes, characterized by almost equal energy content, exists in both cases, suggesting that this phenomenon is robust to the external force on the flow. A relatively concentrated distribution of the flow energy among the modes is observed for the controlled case, since only the first three modes already approach 95% of the total energy, while for the uncontrolled case the cumulative energy of the same number of modes is approximately 2% lower. This may indicate that the rotating rod brings coherence to the dominant flow structures. The phase portraits of POD coefficients for the first three mode pairs are shown in Fig. 17. The first noticeable distinction is that the trajectory is more repeatable in the controlled case, especially for the higher modes. Such a repeatability implies a stronger connection and a more prominent pairing process between two modes. Moreover, though both display a circular pattern, the radius

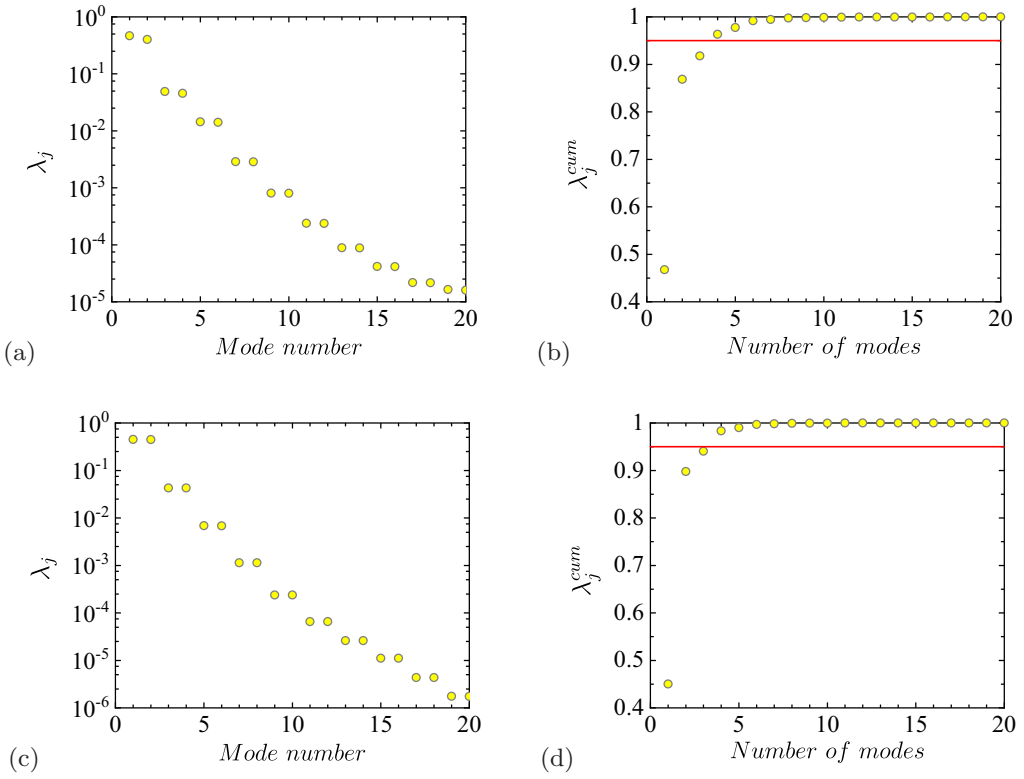

FIG. 16. Distribution of modal energy for an SD7003 airfoil, for (a, b) the uncontrolled case with $\alpha = 8^\circ$ and (c, d) the optimal controlled case with $l/c = 0.3$, $\xi = 4$, $\alpha = 8^\circ$. In each case the relative energy of POD modes, λ_j, is visualized on the left, while the cumulative energy, λ_j^{cum}, is visualized on the right.

of the controlled case is considerably smaller, highlighting the effectiveness of the rotating rod on suppression of the streamwise velocity fluctuation.

Figure 18 shows contours of streamwise velocity of the first four POD modes. For the uncontrolled case, large-scale coherent structures are present in the first mode pair (modes 1 and 2), which appears as a phase-shifted version of each other. Modes 3 and 4, with half the streamwise wavelength of mode 1, are higher harmonics of the first mode pair. It is interesting to note that modal

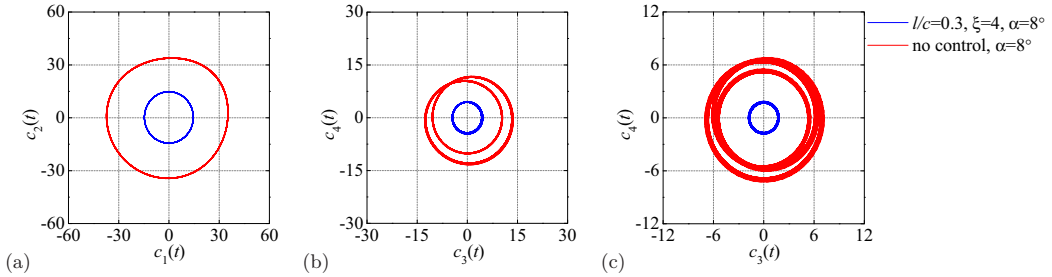

FIG. 17. The phase portraits of POD coefficients for the uncontrolled case with $\alpha = 8^\circ$ (red) and the optimal controlled case with $l/c = 0.3$, $\xi = 4$, $\alpha = 8^\circ$ (blue): (a) the first mode pair c_1 vs c_2, (b) the second mode pair c_3 vs c_4, and (c) the third mode pair c_5 vs c_6.

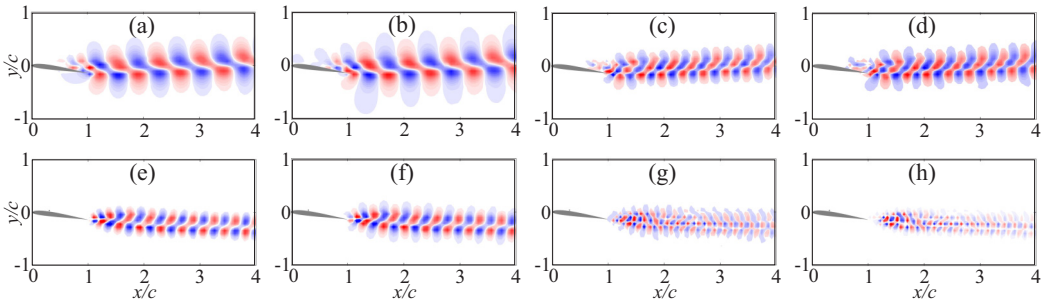

FIG. 18. Contours of streamwise velocity of the first four POD modes for the uncontrolled case with $\alpha = 8^\circ$ (upper row) and the optimal controlled case with $l/c = 0.3$, $\xi = 4$, $\alpha = 8^\circ$ (lower row): (a, e) mode 1, (b, f) mode 2, (c, g) mode 3, and (d, h) mode 4.

structures deflect upwards as they advect downstream. Clearly, this correlates with the P shedding pattern observed in the wake of the plain airfoil. On the other hand, for the optimal control case, the first mode pair and its higher harmonics are featured by the downward skewed structures, thus confirming the transition from a P to 2S wake pattern triggered by a rotating rod with $l/c = 0.3$ and $\xi = 4$. Unlike the former case where the modal structure covers part of the airfoil surface, by this

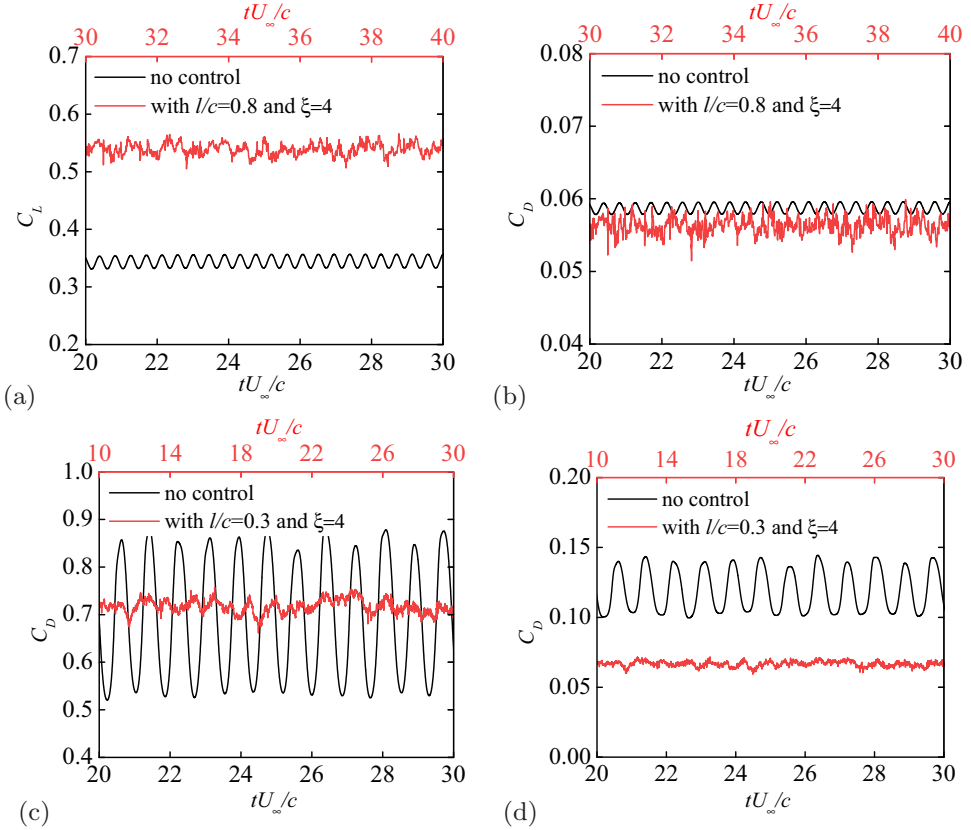

FIG. 19. (a, c) The lift and (b, d) drag coefficient of an SD7003 airfoil for two representative cases at Re = 5000: (a, b) $\alpha = 4^\circ$, $l/c = 0.8$, $\xi = 4$ and (c, d) $\alpha = 8^\circ$, $l/c = 0.3$, $\xi = 4$.

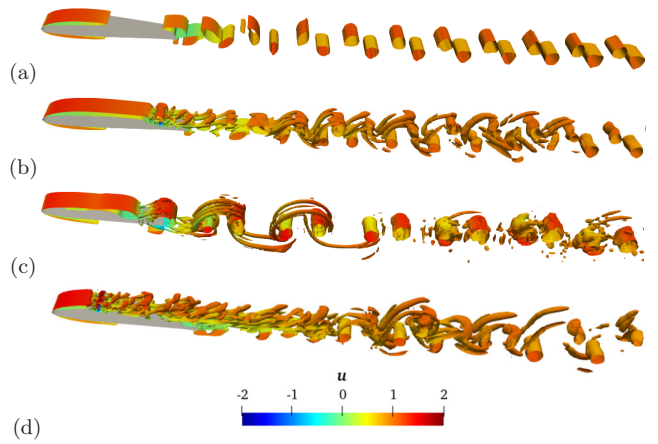

FIG. 20. The instantaneous flow visualization using Q-criterion for an SD7003 airfoil at Re = 5000 (isosurface of $Qc^2/{U_\infty}^2 = 2$ colored by the streamwise velocity): (a) the uncontrolled case with $\alpha = 4^\circ$, (b) the controlled case with $l/c = 0.8$, $\xi = 4$, $\alpha = 4^\circ$, (c) the uncontrolled case with $\alpha = 8^\circ$, and (d) the controlled case with $l/c = 0.3$, $\xi = 4$, $\alpha = 8^\circ$.

control it sets out to make its appearance behind the trailing edge, which indicates that flow around the airfoil is now stabilized and the onset of the velocity fluctuation is postponed downstream.

IV. NUMERICAL RESULTS OF THREE-DIMENSIONAL FLOWS

Three-dimensional numerical simulations were performed to examine the control effects of the rotating rod with the occurrence of spanwise effects in flow dynamics. Figure 19 presents the time history of drag and lift coefficients for two representative cases at $\alpha = 4^\circ$ and 8°. The data for the reference case without a control rod are also included for the sake of comparison. The statistical results show that for the controlled case at $\alpha = 4^\circ$ the time-averaged lift coefficient is increased by 58.5% while the counterpart of drag is decreased by 5.1% with respect to the uncontrolled case. The lift-to-drag ratio is increased by 67%, which is a little higher than that obtained in two-dimensional simulations (56.2%). For the case at $\alpha = 8^\circ$, the control rod has restricted effects on the lift force; however, a significant drag reduction results in an increase of the lift-to-drag ratio by 82.7%, which is close to that for two-dimensional simulation (86.5%). In addition, the hydrodynamic force fluctuations are also apparently inhibited, particularly at a higher attack angle of $\alpha = 8^\circ$. These results verify an improved aerodynamic performance with the consideration of three-dimensional effects.

The influence of the control rod on development of a three-dimensional wake structure is illustrated in Fig. 20. As shown in this figure, for the uncontrolled case at $\alpha = 4^\circ$ the wake is primarily two-dimensional; however, the control rod triggers three-dimensional instabilities, which grow in the boundary layer at the downstream side of the control rod. This is expected because momentum injected into this region makes the boundary layer much more energetic and accordingly, wake transition occurs. A similar behavior can be induced at $\alpha = 8^\circ$, for which the shear layer instability with the control rod occurs at a much earlier position as compared with that of the uncontrolled case.

V. CONCLUSION

Two-dimensional numerical simulations employing a high-order spectral element method are presented to investigate wake suppression effects of a rotating rod on low-Reynolds-number

aerodynamics of an SD7003 airfoil. The study mainly focuses on revealing the variation of aerodynamic performance due to the presence of a rotating rod in the boundary layer of the suction side for different attack angles. In addition, three-dimensional simulations are also performed to examine the influence of spanwise effects. The main findings of this study are summarized below:

Four different wake modes, respectively, of steady, 2S, P, and P+S are observed with the variation of rod location and rotational speed. The associated distribution of the wake modes is mapped in the $(\xi, l/c)$ plane at $\alpha = 4^\circ$ and 8°. For the case with $\alpha = 4^\circ$, a steady mode widely occupies the upper right region while the P and P+S modes are available at the lower left corner of the plane. The 2S mode fills out the area of the remaining region in the $(\xi, l/c)$ plane. In comparison, the $(\xi, l/c)$ plane for $\alpha = 8^\circ$ is divided into two different unsteady modes of 2S and P+S, respectively. In contrast to the case at $\alpha = 4^\circ$, the 2S mode shifts from the lower right corner to the upper left corner at $\alpha = 8^\circ$. In addition, of the region the P+S mode occupies is enlarged noticeably when the attack angle increases from 4° to 8°.

Statistical results of the aerodynamic forces are yielded in terms of mean and fluctuating components of drag and lift force and lift-to-drag ratio as well. A pronounced increase of the lift-to-drag ratio is observed for both attack angles 4° and 8°, which are in line with the wake mode transition from an unsteady wake of 2S to a steady (or weakly shedding) mode at $\alpha = 4^\circ$ and from the P+S mode to 2S (or P) mode at 8°. Contribution of the lift enhancement and drag reduction to the aerodynamic performance varies according to the variation of attack angle. The control efficiency is also evaluated with account of the external power consumed in the rod rotation, showing promising effectiveness even at moderate rotational speeds.

We also apply POD to the computed streamwise velocity field, whereby the distinct wake modes, 2S and P modes, are faithfully correlated with the corresponding dominant modes. Furthermore, the POD results reveal that (i) the rotating rod is favorable for lowering the fluctuation of streamwise velocity, and (ii) the rotating rod is able to stabilize the flow around the airfoil and postpone the velocity fluctuation further downstream.

Three-dimensional numerical simulations are supplemented to corroborate the 2D results. It should be noted that the control performance of the rotating rod deteriorates when the attack angle further increases because of massive flow separation from the leading edge of the airfoil. Multiple rotating rods may be considered to ameliorate the aerodynamic performance at higher attack angles, which will be studied in our future research. In addition, optimization of geometrical parameters such as gap spacing and control rod diameter with respect to the chord length are also critical issues which need to be prioritized in our work.

ACKNOWLEDGMENTS

Financial support from the National Natural Science Foundation of China (Grants No. 11772193, No. 51879160, and No. 52101322), the Innovation Program of the Shanghai Municipal Education Commission (Grant No. 2019-01-07-00-02-E00066), the Program for Intergovernmental International S&T Cooperation Projects of Shanghai Municipality (Grant No. 18290710600), the Oceanic Interdisciplinary Program of Shanghai Jiao Tong University (Grant No. SL2020PT201), and the China Postdoctoral Science Foundation (Grants No. 2020M671128 and No. 2020TQ0192) is gratefully acknowledged.

[1] D. J. Pines and F. Bohorquez, Challenges facing future micro-air-vehicle development, J. Aircr. **43**, 290 (2006).

[2] R. Wood, B. Finio, M. Karpelson, K. Ma, and J. Whitney, Progress on 'pico' air vehicles, Int. J. Rob. Res. **31**, 1292 (2012).

[3] L. Petricca, P. Ohlckers, and C. Grinde, Micro- and nano-air vehicles: State of the art, Int. J. Aerosp. Eng. **2011**, 214549 (2011).

[4] T. J. Mueller, *Fixed and Flapping Wing Aerodynamics for Micro Air Vehicle Applications* (American Institute of Aeronautics and Astronautics, Reston, VA, 2001).
[5] T. J. Mueller and J. D. DeLaurier, Aerodynamics of small vehicles, Annu. Rev. Fluid Mech. **35**, 89 (2003).
[6] K. Takizawa, T. E. Tezduyar, and N. Kostov, Sequentially-coupled space-time FSI analysis of bio-inspired flapping-wing aerodynamics of an MAV, Comput. Mech. **54**, 213 (2014).
[7] K. Takizawa, T. E. Tezduyar, and A. Buscher, *Space-Time Computational Analysis of MAV Flapping-Wing Aerodynamics with Wing Clapping* (Springer, Berlin, Heidelberg, 2015), pp. 1–11.
[8] M. Abas, A. Rafie, H. B. Yusoff, and K. Ahmad, Flapping wing micro-aerial-vehicle: Kinematics, membranes, and flapping mechanisms of ornithopter and insect flight, Chin. J. Aeronaut. **29**, 1159 (2016).
[9] Q. Wen, S. Guo, H. Li, and W. Dong, Nonlinear dynamics of a flapping rotary wing: Modeling and optimal wing kinematic analysis, Chin. J. Aeronaut. **31**, 1041 (2018).
[10] Kesel and B. Antonia, Aerodynamic characteristics of dragonfly wing sections compared with technical aerofoils, J. Exp. Biol. **203**, 3125 (2000).
[11] J. T. Murphy and H. Hui, An experimental study of a bio-inspired corrugated airfoil for micro air vehicle applications, Exp. Fluids **49**, 531 (2010).
[12] G. Luo and S. Mao, The effects of corrugation and wing planform on the aerodynamic force production of sweeping model insect wings, Acta Mech. Sin. **21**, 531 (2005).
[13] H. Tang, Y. Lei, X. Li, K. Gao, Y. Li, and E. Sciubba, Aerodynamic shape optimization of a wavy airfoil for ultra-low Reynolds number regime in gliding flight, Energies **13**, 467 (2020).
[14] D. F. Mateescu, A. Panahi, and V. Roy, Analysis of the flow past airfoils with gurney flaps at low Reynolds numbers, in *52nd Aerospace Sciences Meeting* (AIAA, National Harbor, MD, 2014), p. 0040.
[15] M. Gopalakrishnan Meena, K. Taira, and K. Asai, Airfoil-wake modification with gurney flap at low Reynolds number, AIAA J. **56**, 1348 (2018).
[16] Z. Fang, C. Gong, A. Revell, G. Chen, A. Harwood, and J. Oconnor, Passive separation control of a NACA0012 airfoil via a flexible flap, Phys. Fluids **31**, 101904 (2019).
[17] A. Favre, *Contribution à l'étude Expérimentale des Mouvements Hydrodynamiques à deux Dimensions* (E. Blondel La Rougery, 1938), Vol. 137.
[18] V. Modi, F. Mokhtarian, M. Fernando, and T. Yokomizo, Moving surface boundary-layer control as applied to two-dimensional airfoils, J. Aircr. **28**, 104 (1991).
[19] A. Z. Al-Garni, A. M. Al-Garni, S. A. Ahmed, and A. Z. Sahin, Flow control for an airfoil with leading-edge rotation: An experimental study, J. Aircr. **37**, 617 (2000).
[20] X. Du, T. Lee, F. Mokhtarian, and F. Kafyeke, Flow past an airfoil with a leading-edge rotation cylinder, J. Aircr. **39**, 1079 (2002).
[21] P. Gerontakos and T. Lee, Near wake behind an airfoil with leading-edge flow control, J. Aircr. **42**, 561 (2005).
[22] H. Zhu, Simultaneous CFD evaluation of VIV suppression using smaller control cylinders, J. Fluids Struct. **57**, 66 (2015).
[23] I. Korkischko and J. R. Meneghini, Suppression of vortex-induced vibration using moving surface boundary-layer control, J. Fluids Struct. **34**, 259 (2012).
[24] S. Mittal, Control of flow past bluff bodies using rotating control cylinders, J. Fluids Struct. **15**, 291 (2001).
[25] J. C. Schulmeister, J. Dahl, G. Weymouth, and M. Triantafyllou, Flow control with rotating cylinders, J. Fluid Mech. **825**, 743 (2017).
[26] Z. Yu, H. Ping, X. Liu, H. Zhu, R. Wang, Y. Bao, D. Zhou, Z. Han, and H. Xu, Turbulent wake suppression of circular cylinder flow by two small counter-rotating rods, Phys. Fluids **32**, 115123 (2020).
[27] M. Galbraith and M. Visbal, Implicit large eddy simulation of low Reynolds number flow past the SD7003 airfoil, in *46th AIAA Aerospace Sciences Meeting and Exhibit* (2008).
[28] M. R. Visbal, R. E. Gordnier, and M. C. Galbraith, High-fidelity simulations of moving and flexible airfoils at low Reynolds numbers, Exp. Fluids **46**, 903 (2009).
[29] V. Golubev, T. Hollenshade, L. Nguyen, and M. Visbal, Parametric viscous analysis of gust interaction with SD7003 airfoil, *48th AIAA Aerospace Sciences Meeting Including the New Horizons Forum and Aerospace Exposition, Orlando, Florida* (2010), p. 928.

[30] L. Nguyen, V. V. Golubev, and M. R. Visbal, Numerical study of transitional SD7003 airfoil interacting with canonical upstream flow disturbances, AIAA J. **56**, 158 (2018).

[31] C. D. Cantwell, D. Moxey, A. Comerford, A. Bolis, G. Rocco, G. Mengaldo, D. De Grazia, S. Yakovlev, J.-E. Lombard, D. Ekelschot *et al.*, Nektar++: An open-source spectral/hp element framework, Comput. Phys. Commun. **192**, 205 (2015).

[32] G. Karniadakis and S. Sherwin, *Spectral/hp Element Methods for Computational Fluid Dynamics* (Oxford University Press, Oxford, England, 2013).

[33] A. Uranga, P. O. Persson, M. Drela, and J. Peraire, Implicit large eddy simulation of transition to turbulence at low Reynolds numbers using a discontinuous Galerkin method, Int. J. Numer. Methods Eng. **87**, 232 (2011).

[34] A. Ducoin, J.-C. Loiseau, and J.-C. Robinet, Numerical investigation of the interaction between laminar to turbulent transition and the wake of an airfoil, Eur. J. Mech. B. Fluids **57**, 231 (2016).

[35] C. H. Williamson and A. Roshko, Vortex formation in the wake of an oscillating cylinder, J. Fluids Struct. **2**, 355 (1988).

[36] D. F. Kurtulus, On the unsteady behavior of the flow around NACA 0012 airfoil with steady external conditions at Re = 1000, Int. J. Micro Air Veh. **7**, 301 (2015).

[37] H. Ping, H. Zhu, K. Zhang, R. Wang, and Z. Han, Wake dynamics behind a rotary oscillating cylinder analyzed with proper orthogonal decomposition, Ocean Eng. **218**, 108185 (2020).